Low-frequency beamforming for a miniaturized aperture three-by-three uniform rectangular array of acoustic vector sensors[a)]

Xijing Guo[b)]
School of Marine Science and Technology, Northwestern Polytechnical University, 127 West Youyi Road, Xi'an, 710072, China

Shi'e Yang[c)]
College of Underwater Acoustic Engineering, Harbin Engineering University, 145 Nantong Street, Harbin, 150001, China

Sebastian Miron
Université de Lorraine, CRAN, UMR 7039, Vandœuvre-lès-Nancy, F-54506, France

(Received 18 August 2015; revised 27 October 2015; accepted 26 November 2015; published online 24 December 2015)

This paper proposes a mode domain beamforming method for a 3×3 uniform rectangular array of two-dimensional (2D) acoustic vector sensors with inter-sensor spacing much smaller than the wavelengths in the working frequency band. The acoustic modes are extracted from the particle velocity observations in light of the source-sink pictures of the Taylor's series multipoles [Wikswo and Swinney, J. Appl. Phys. **56**(11), 3039–3049 (1984)]. Then, similar to other mode domain methods, the modes are synthesized to obtain the desired beam pattern. The proposed method is limited to the cases where five is the maximum order of the modes for pattern synthesis, meaning that the directivity index in the 2D isotropic noise case can reach up to 10.4 dB. The proposed method has been validated by field experiments. © *2015 Acoustical Society of America*.
[http://dx.doi.org/10.1121/1.4937759]

[MRB] Pages: 3873–3883

I. INTRODUCTION

The mode domain beamforming has become a widely used technique in the design of superdirective microphone arrays of spherical,[1–5] circular,[6,7] and linear apertures.[8–11] Other than these microphone applications, this method is also useful to develop superdirective hydrophone arrays with miniaturized aperture.[12–15] Such a technique is referred to as "mode domain" processing because it is based on the decomposition of the soundfield measurements into a series of acoustic modes of different orders, i.e., the eigenfunctions of the wave equation; the obtained acoustic modes are then synthesized to fit the desired beam pattern.

A superdirective sensor array can be regarded from an alternative perspective as a realization of the concept "higher order acoustic sensor."[16–18] In this sense, due to its dipole behavior, a particle velocity sensor is a first order acoustic sensor. A particle velocity sensor can be physically implemented by an accelerometer or by a subtractive array of two closely positioned pressure sensors, which provides the spatial gradient of the pressure. An acoustic vector sensor (AVS) is usually composed of two or three collocated and orthogonally oriented particle velocity sensors and possibly an acoustic pressure sensor. It has been shown experimentally that the AVS is advantageous over the omnidirectional pressure sensor as it presents an increased gain against the ambient noise and a higher angular resolution in virtue of the directional capabilities of particle velocity sensors.[19–23]

Superdirectivity can be achieved by using an array of AVS subject to stringent constraints on the aperture. The uniform circular array (UCA) of two-dimensional (2D) AVS[24] is such an example. The 2D AVS refers to an AVS consisting of only two independent particle velocity sensors. Such a device is capable of measuring two of the three orthogonal components of the particle velocity of the acoustic wave. A superdirective beamformer has also been proposed for the short uniform linear array (ULA) of 2D AVS.[25] Unlike most superdirective ULAs that only comprise the pressure sensors, the main response axis of this superdirective ULA of 2D AVS can be freely steered to any direction in the 2D space.

This paper introduces a superdirective mode domain beamformer for a 3×3 uniform rectangular array (URA) of 2D AVS with miniaturized aperture. Similar to Gur's ULA,[25] the proposed beamformer design is also based on the finite differences of the particle velocity measurements for the extraction of the acoustic modes. The differential coefficients are obtained in light of the source-sink pictures of the

[a)]Some results of this work were presented in "A low-frequency superdirective acoustic vector sensor array," in Proceedings of IEEE International Conference on Acoustics, Speech and Signal Processing, Brisbane, Australia, April 2015.

[b)]Also at: State Key Laboratory of Acoustics, Institute of Acoustics, Chinese Academy of Sciences, Beijing 100190, China. Electronic mail: xguo@nwpu.edu.cn

[c)]Also at: School of Marine Science and Technology, Northwestern Polytechnical University, 127 West Youyi Road, 710072 Xi'an, China.

Taylor's series dipole, quadrupole, and multipoles of higher orders.[26] Field experiments have been carried out to test and validate the proposed approach. The results show that, despite its miniaturized aperture, the 3×3 array is superdirective and the synthesized beam patterns are frequency invariant over a broad band of several hundreds of hertz. The miniaturized aperture makes this array attractive for easy deployment and maintenance at sea, with possible applications in underwater acoustic surveillance such as target detection and direction of arrival (DOA) estimation.

II. SUPERDIRECTIVE BEAMFORMER FOR THE URA

A. The URA

Consider the 3×3 URA of 2D AVS with inter-sensor spacing a shown in Fig. 1, where a 2D Cartesian coordinate system is also established with the origin coinciding with the center of the array. Other than the uniform grid where the 2D AVSs are positioned, by "uniform" we also mean that the main response axes of the two particle velocity sensors of these 2D AVSs are uniformly aligned along the x and the y directions, providing observations of the two horizontal particle velocity components of the incident acoustic wave. In addition to the nine 2D AVSs, an omnidirectional pressure sensor is placed at the center of the array. A low-frequency acoustic plane wave arrives on the array at velocity c from angle ϕ, measured from the positive x axis. Herein, by "low-frequency," we mean that $a/\lambda \ll 1$, where λ denotes the wavelength.

Note that the pressure sensor and the particle velocity sensor are different types of sensors. The sensitivity of the pressure sensor is defined in terms of the sound pressure, which is not the case for the particle velocity sensor. Suppose, without loss of generality, that the pressure measured at the position (x,y) has unit magnitude and is given by

$$p(x,y) = e^{jk(x\cos\phi + y\sin\phi)},$$

where $j = \sqrt{-1}$ and $k = 2\pi/\lambda$ denotes the wavenumber. The time dependent part $e^{j\omega t}$, where $\omega = kc$ is the angular frequency, has been omitted for simplicity. Accordingly, from the two channels of the vector sensor, at the same point of coordinates (x,y), we obtain

$$\begin{aligned} v_x(x,y) &= Ve^{jk(x\cos\phi + y\sin\phi)}\cos\phi, \\ v_y(x,y) &= Ve^{jk(x\cos\phi + y\sin\phi)}\sin\phi, \end{aligned} \tag{1}$$

where V is the amplitude of the particle velocity measurements. In this paper, we assume, without loss of generality, that the sensitivities of the pressure and the particle velocity sensors are equivalent. This means that, for a given incident wave, if the main response axis of the particle velocity sensor coincides with the direction of the incident wave, the outputs of the pressure sensor and the particle velocity sensor are the same. In practice, this can always be obtained by properly scaling the particle velocity measurements to have $V = 1$. Under these circumstances, the array response can be expressed as a $(2L+1) \times 1$ vector

$$\mathbf{v}(\phi) = [1 \quad \mathbf{a}^T(\phi)\cos\phi \quad \mathbf{a}^T(\phi)\sin\phi]^T, \tag{2}$$

with $L = 9$, where the operator $(\cdot)^T$ denotes the matrix transpose. The scalar "1" corresponds to the pressure measurement and the other entries of $\mathbf{v}(\phi)$ to the particle velocity measurements. The ℓth element of the vector $\mathbf{a}(\phi)$ is given by $a_\ell(\phi) = e^{jk(x_\ell\cos\phi + y_\ell\sin\phi)}$, where

$$x_\ell = \begin{cases} -a, & \ell = 1,2,3; \\ 0, & \ell = 4,5,6; \\ a, & \ell = 7,8,9; \end{cases}$$

$$y_\ell = \begin{cases} a, & \ell = 1,4,7; \\ 0, & \ell = 2,5,8; \\ -a, & \ell = 3,6,9. \end{cases}$$

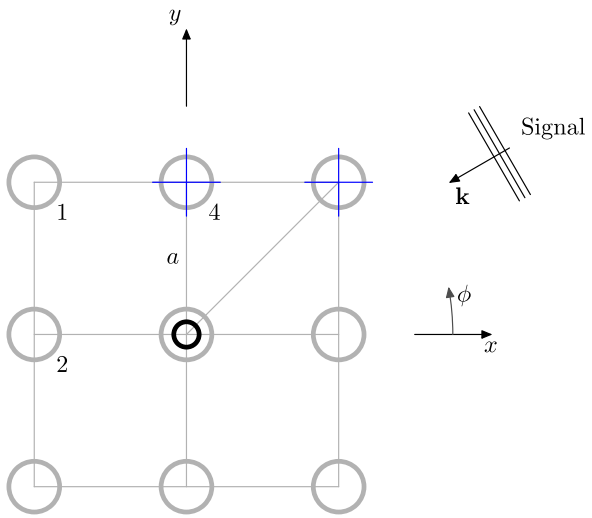

FIG. 1. (Color online) Top view of the vector sensor array. A gray circle denotes a 2D vector sensor whereas the smaller dark circle denotes an omnidirectional pressure sensor. The blue cross on the gray circle denotes the orientations of the two main response axes of a 2D AVS.

B. The mode domain beamformer

The wavefield can be decomposed into a series of acoustic modes of different orders, also known as the multipole expansion.[26] In this paper, we are only interested in the azimuth-dependent component of these modes. The 0th order mode is azimuth independent and can be simply denoted by one. The 1st, 2nd, 3rd, and higher order modes correspond to dipole, quadrupole, octapole, etc. These modes have a cosine component $\cos n\phi$ and a sine component $\sin n\phi$, for $1 \le n \le N$, where N is the highest order of the available modes. We define the vector of modes

$$\mathbf{b}(\phi) = [1 \quad \mathbf{b}_1^T(\phi) \quad \mathbf{b}_2^T(\phi)]^T,$$

where

$$\mathbf{b}_1(\phi) = \begin{bmatrix} \cos\phi \\ \cos 2\phi \\ \vdots \\ \cos N\phi \end{bmatrix}, \quad \mathbf{b}_2(\phi) = \begin{bmatrix} \sin\phi \\ \sin 2\phi \\ \vdots \\ \sin N\phi \end{bmatrix}.$$

Once $\mathbf{b}(\phi)$ is obtained from the data, the pattern synthesis step is very similar to the conventional ULA processing.[27] For example, if we choose

$$\bar{\mathbf{b}}(\varphi) = \frac{1}{2N+1}\begin{bmatrix} 1 & 2\mathbf{b}_1^T(\varphi) & 2\mathbf{b}_2^T(\varphi) \end{bmatrix}$$

as the steering vector (where φ is the steering angle), the beam pattern is given by

$$\mathcal{B}(\phi) = \bar{\mathbf{b}}^T(\varphi)\mathbf{b}(\phi) = 1 + 2\sum_{n=1}^{N} \cos\, n(\varphi - \phi) = \sum_{n=-N}^{N} e^{jn(\phi-\varphi)}. \tag{3}$$

Observing the similarities between the last term and the array response of the uniformly weighted ULA of $2N+1$ elements, we obtain[27]

$$\mathcal{B}(\phi) = \frac{1}{2N+1}\frac{\sin\frac{2N+1}{2}(\varphi-\phi)}{\sin\frac{1}{2}(\varphi-\phi)}. \tag{4}$$

If a different steering vector $\bar{\mathbf{b}}(\varphi)$ is used, the beam pattern changes; see Ref. 25, for example. However, since the pattern synthesis is analogous to the ULA case, in this paper, we will focus on how to estimate the mode components $\mathbf{b}(\phi)$ for the 3×3 2D-AVS URA.

It should be pointed out that there exist some other beamforming methods for superdirectivity where the pattern synthesis step is completely different from the conventional ULA case. The method of Ref. 28 is such an example; therein superdirectivity can be achieved without the effort of estimating the mode components. Instead, the approach in Ref. 28 requires *a priori* knowledge of the DOA of the incident wave.

In Secs. II C–II E, we propose a method for obtaining the acoustic modes of orders $1-N$ from the incident wave measurements made by this 3×3 2D-AVS URA. This method consists of three steps: the mode extraction, the amplification, and the decoupling. These steps establish a link between the array response $\mathbf{v}(\phi)$ and the vector of modes $\mathbf{b}(\phi)$. Then the pattern synthesis step [Eq. (3)] can be used to obtain the desired beam pattern in a similar way to the conventional ULA case. The mode beamformer filter weights $\mathbf{w}(\varphi)$ are those satisfying $\mathcal{B}(\phi) = \mathbf{w}(\varphi)^H\mathbf{v}(\phi) \approx \bar{\mathbf{b}}^T(\varphi)\mathbf{b}(\phi)$.

C. The mode extraction

The main reason for having a pressure sensor positioned at the center of the 2D-AVS URA is to directly obtain the measurements of the 0th order acoustic mode due to the omnidirectional property of the pressure sensor.

For the modes of order $n \geq 1$, the outputs of the 2D AVS are multiplied by some constant coefficients and summed up to produce the finite differences of the particle velocities. The nth order finite difference of the particle velocities are denoted by $u_p^{(n)}$ for $p=1,2$, each corresponding to one of the two mode components $\cos n\phi$ and $\sin n\phi$. It should be pointed out that the nth order finite difference may not necessarily be exactly the nth order mode, but it contains the nth order mode, as will be shown in the sequel. We denote by $v_{\ell,x}$ and $v_{\ell,y}$ the the particle velocity observations made by the two channels of the ℓth 2D AVS, for $\ell \in \mathcal{L} = \{1,\ldots,9\}$, which are the $(\ell+1)$th and the $(\ell+L+1)$th elements of $\mathbf{v}(\phi)$, respectively [see Eq. (2) for the definition of $\mathbf{v}(\phi)$]. The finite differences can then be formulated as

$$\begin{aligned} u_1^{(n)} &= \sum_\ell g_{\ell,1}^{(n)} v_{\ell,x} + \sum_\ell g_{\ell,2}^{(n)} v_{\ell,y}, \\ u_2^{(n)} &= -\sum_\ell g_{\ell,2}^{(n)} v_{\ell,x} + \sum_\ell g_{\ell,1}^{(n)} v_{\ell,y}, \end{aligned} \tag{5}$$

where $g_{\ell,q}^{(n)}$ is the constant coefficient associated with the ℓth 2D AVS for the nth order finite differences. Two sets of coefficients $\mathcal{S}_q^{(n)} = \{g_{\ell,q}^{(n)}, \ell \in \mathcal{L}\}$ are used for both channels of the 2D AVS simultaneously, where the subscript $q=1,2$ is used to indicate the two sets. Substituting Eq. (2) into Eq. (5), we further obtain

$$\begin{bmatrix} u_1^{(n)} \\ u_2^{(n)} \end{bmatrix} = \begin{bmatrix} \sum_\ell g_{\ell,1}^{(n)} a_\ell(\phi) & \sum_\ell g_{\ell,2}^{(n)} a_\ell(\phi) \\ -\sum_\ell g_{\ell,2}^{(n)} a_\ell(\phi) & \sum_\ell g_{\ell,1}^{(n)} a_\ell(\phi) \end{bmatrix} \begin{bmatrix} \cos\phi \\ \sin\phi \end{bmatrix}. \tag{6}$$

In the subsequent discussions, the 2×2 matrix in Eq. (6) will be denoted by $\mathbf{M}^{(n)}$ for the nth order finite difference. It can be observed from Eq. (6) that the elements of $\mathbf{M}^{(n)}$, say, $m_{ij}^{(n)}$, $i,j \in \{1,2\}$, satisfy

$$m_{11}^{(n)} = m_{22}^{(n)},\ m_{12}^{(n)} = -m_{21}^{(n)}. \tag{7}$$

We choose the finite difference coefficients $g_{\ell,q}^{(n)}$ based on the Taylor's series multipoles described by the pictures of point sources and sinks.[26] Figure 2 shows the 2D-AVS URA with different sets of differential coefficients in analogy to the corresponding source-sink pictures of the multipoles. Appendix A provides the detailed derivation of the finite differences by order.

In summary, for each $n \leq N \leq 5$, we can derive a pair of nth order differentials of the particle velocities $u_1^{(n)}$ and $u_2^{(n)}$. These differentials are grouped by order to form a $(2N+1)\times 1$ vector

$$\mathbf{u} = [\,1 \quad u_1^{(1)} \quad \cdots \quad u_1^{(N)} \quad u_2^{(1)} \quad \cdots \quad u_2^{(N)}\,]^T. \tag{8}$$

The element "1" in $\mathbf{u}$ denotes the normalized amplitude of the pressure, which provides the 0th order mode. Then, the mode extraction step can be concisely expressed by

$$\mathbf{u} = \mathbf{G}\mathbf{v}(\phi). \tag{9}$$

The $(2N+1)\times(2L+1)$ matrix $\mathbf{G}$ can be partitioned into blocks as

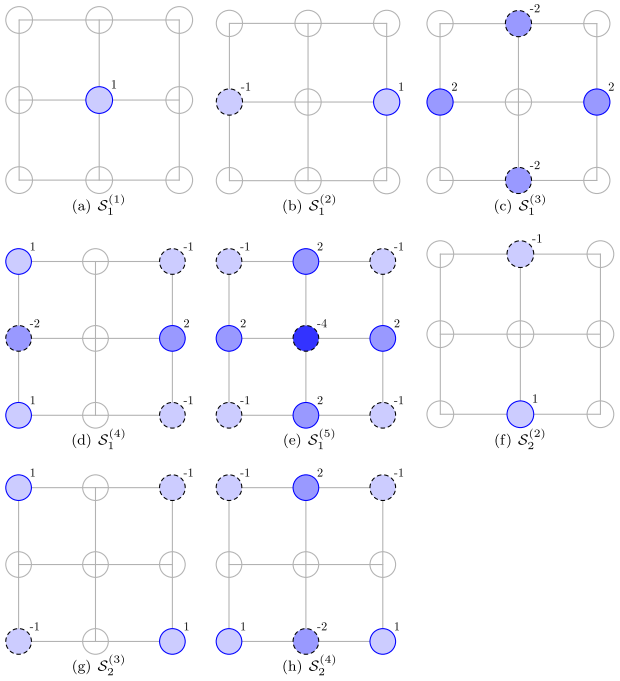

FIG. 2. (Color online) Illustration of the 2D AVSs with their respective coefficients. (a)–(e) illustrate one set of the coefficients for all the 5 modes. (f)–(h) illustrate the other set of the coefficients for the modes of orders 2–4. The highlighted circles denote the 2D AVS with nonzero coefficients. The digit to the upper right of the 2D AVS is the coefficient associated with it, where the sensor with a positive coefficient is marked by the solid circle and the sensor with a negative weight is marked by the dashed circle.

$$\mathbf{G} = \begin{bmatrix} 1 & & \\ & \mathbf{G}_1 & \mathbf{G}_2 \\ & -\mathbf{G}_2 & \mathbf{G}_1 \end{bmatrix},$$

where the (n, ℓ) elements of the subblocks $\mathbf{G}_1$ and $\mathbf{G}_2$ are, respectively, given by the coefficients $g_{\ell,1}^{(n)}$ and $g_{\ell,2}^{(n)}$. If $N=5$, the two subblocks $\mathbf{G}_1$ and $\mathbf{G}_2$ are given by

$$\mathbf{G}_1 = \begin{bmatrix} 0 & 0 & 0 & 0 & 1 & 0 & 0 & 0 & 0 \\ 0 & -1 & 0 & 0 & 0 & 0 & 0 & 1 & 0 \\ 0 & 2 & 0 & -2 & 0 & -2 & 0 & 2 & 0 \\ 1 & -2 & 1 & 0 & 0 & 0 & -1 & 2 & -1 \\ -1 & 2 & -1 & 2 & -4 & 2 & -1 & 2 & -1 \end{bmatrix}$$

and

$$\mathbf{G}_2 = \begin{bmatrix} 0 & 0 & 0 & 0 & 0 & 0 & 0 & 0 & 0 \\ 0 & 0 & 0 & -1 & 0 & 1 & 0 & 0 & 0 \\ 1 & 0 & -1 & 0 & 0 & 0 & -1 & 0 & 1 \\ -1 & 0 & 1 & 2 & 0 & -2 & -1 & 0 & 1 \\ 0 & 0 & 0 & 0 & 0 & 0 & 0 & 0 & 0 \end{bmatrix}.$$

The nth rows are associated with the nth order finite differentials. For the cases $N<5$, both subblocks are simply substituted by their first N rows.

Furthermore, it can be easily shown, using the equations of Appendix A, that the relationship between the vector of modes $\mathbf{b}(\phi)$ and the vector $\mathbf{u}$ is given by

$$\mathbf{u} \approx \mathbf{K}(\mathbf{R}\mathbf{b}(\phi) + \mathbf{z}). \tag{10}$$

In the above equation, the $(2N+1)\times(2N+1)$ matrix $\mathbf{R}$ can be expressed as

$$\mathbf{R} = \begin{bmatrix} 1 & & \\ & \mathbf{R}_1 & \\ & & \mathbf{R}_2 \end{bmatrix}. \tag{11}$$

For $N=5$, the two subblocks are

$$\mathbf{R}_1 = \begin{bmatrix} 1 & & & & \\ 0 & 1 & & & \\ 0 & 0 & 1 & & \\ 0 & 0 & 0 & 1 & \\ -2 & 0 & 1 & 0 & 1 \end{bmatrix},$$

$$\mathbf{R}_2 = \begin{bmatrix} 1 & & & & \\ 0 & 1 & & & \\ 0 & 0 & 1 & & \\ 0 & 0 & 0 & 1 & \\ -2 & 0 & -1 & 0 & 1 \end{bmatrix}.$$

Observe that $\mathbf{R}_1$ and $\mathbf{R}_2$ are lower triangular matrices, where the (ℓ,k) elements are nonzero *only if* $\ell - k$ is even. The vector $\mathbf{z}$ is given by $\mathbf{z} = [0 \quad \mathbf{z}_1^T \quad \mathbf{z}_2^T]^T$, where $\mathbf{z}_1 = [0 \quad 0 \quad 0 \quad -1 \quad 0]^T$, whereas $\mathbf{z}_2$ is a 5×1 vector of zeros. The matrix $\mathbf{K}$ is a complex block diagonal matrix

$$\mathbf{K} = \begin{bmatrix} 1 & & \\ & \bar{\mathbf{K}} & \\ & & \bar{\mathbf{K}} \end{bmatrix}, \tag{12}$$

with

$$\bar{\mathbf{K}} = \mathrm{diag}\left(1 \quad \kappa \quad 2\kappa^2 \quad \frac{1}{2}\kappa^3 \quad \frac{1}{16}\kappa^4\right) \text{ and } \kappa = jka.$$

For $N<5$, the matrices $\mathbf{R}_1$, $\mathbf{R}_2$, and $\bar{\mathbf{K}}$ are substituted by their respective upper left subblocks, resulting in three $N\times N$ matrices. In accordance, the first N elements of the vector $\mathbf{z}_1$ form the new vector $\mathbf{z}_1$, and $\mathbf{z}_2$ reduces to an N-element vector of zeros.

So far, we have established a link between $\mathbf{u}$ and $\mathbf{b}(\phi)$. In order to obtain the vector of modes $\mathbf{b}(\phi)$, the beamformer still needs the following two steps.

D. The amplification

Observe that the elements of the diagonal matrix $\mathbf{K}$ are of magnitude $|\kappa|^{n-1}$. Since $|\kappa| = ka < 1$, it means that the amplitudes of these differentials are imbalanced by order. The reason is that the higher order mode components of the incident wave are much weaker than those of lower orders. To compensate this, we introduce the amplification step, which is implemented by multiplying $\mathbf{u}$ by $\mathbf{K}^{-1}$ on the left, yielding

$$\mathbf{h} = \mathbf{K}^{-1}\mathbf{u} \approx \mathbf{R}\mathbf{b}(\phi) + \mathbf{z}. \tag{13}$$

However, it comes at the cost of a sharp decrease in the white noise gain (WNG), which will be shown in Sec. III.

E. The decoupling

As shown in Appendix A, a so-called "coupling" phenomenon between the modes can be observed. That is, in the finite difference terms $u_q^{(n)}$, other than the nth order mode components, there can also be some undesired $(n-2\ell)$th order mode components for $1 \le \ell \le \lfloor n/2 \rfloor$, where $\lfloor \cdot \rfloor$ denotes the integer part of a number. This accounts for the reason that $\mathbf{R}_1$ and $\mathbf{R}_2$ are lower triangular matrices and their (ℓ,k) element is nonzero only if $\ell - k$ is even.

Therefore, a decoupling step is still necessary to resolve the mixture of the modes. We can show that the vector of modes $\mathbf{b}(\phi)$ can be obtained by solving

$$\mathbf{b}(\phi) = \mathbf{D}\mathbf{h} \tag{14}$$

with respect to $\mathbf{D}$, termed as the decoupling matrix, subject to the constraint that the unknown matrix $\mathbf{D}$ is independent of the incidence angle ϕ. We recall that the estimates $u_q^{(n)}$ may contain the 0th order mode only if n is even and $q=1$ (those associated with the cosine mode components). In this case, the pressure observation, which provides an estimate of the 0th order mode, is needed to decouple the mixture of the cosine mode components of even orders.

It can be observed from Eq. (11) that there is no coupling between the cosine and the sine mode components. Hence, we can deduce that $\mathbf{D}$ is also a block diagonal matrix, which can be expressed as

$$\mathbf{D} = \begin{bmatrix} 1 & & \\ \mathbf{d} & \bar{\mathbf{D}} & \\ & & \tilde{\mathbf{D}} \end{bmatrix}. \tag{15}$$

If we substitute Eqs. (15) and (13) into Eq. (14), we obtain the two decoupled equations

$$\mathbf{b}_1(\phi) = \mathbf{d} + \bar{\mathbf{D}}\mathbf{R}_1\mathbf{b}_1(\phi) + \bar{\mathbf{D}}\mathbf{z}_1, \tag{16}$$

$$\mathbf{b}_2(\phi) = \tilde{\mathbf{D}}\mathbf{R}_2\mathbf{b}_2(\phi). \tag{17}$$

A reformulation of Eq. (16) yields

$$\mathbf{d} + \bar{\mathbf{D}}\mathbf{z}_1 + (\bar{\mathbf{D}}\mathbf{R}_1 - \mathbf{I})\mathbf{b}_1(\phi) = 0.$$

In this equation, only $\mathbf{b}_1(\phi)$ is dependent on ϕ. Hence, this equation holds for any ϕ if and only if $\bar{\mathbf{D}} = \mathbf{R}_1^{-1}$. It follows that $\mathbf{d} = -\mathbf{R}_1^{-1}\mathbf{z}_1$. Similarly, we can derive from Eq. (17) that $\tilde{\mathbf{D}} = \mathbf{R}_2^{-1}$, and finally obtain

$$\mathbf{D} = \begin{bmatrix} 1 & & \\ -\mathbf{R}_1^{-1}\mathbf{z}_1 & \mathbf{R}_1^{-1} & \\ & & \mathbf{R}_2^{-1} \end{bmatrix}. \tag{18}$$

Since $\mathbf{R}_1$ and $\mathbf{R}_2$ are lower triangular matrices, the decoupling matrix $\mathbf{D}$ has the following properties:

(1) $\bar{d}_{\ell,k} = 0$ for $\ell > k$, where $\bar{d}_{\ell,k}$ denotes the typical element of $\bar{\mathbf{D}}$, i.e., $\bar{\mathbf{D}}$ is a lower triangular matrix.
(2) $\bar{d}_{\ell,k} \neq 0$ only if $\ell - k$ is even (see Appendix B for the proof).
(3) $\bar{d}_{\ell,\ell} = 1$.
(4) The properties (1)–(3) also apply to $\tilde{\mathbf{D}}$.

At this stage, we have obtained $\mathbf{b}(\phi) \approx \mathbf{D}\mathbf{K}^{-1}\mathbf{G}\mathbf{v}(\phi)$ after the mode extraction, amplification, and decoupling steps. By substituting $\mathbf{b}(\phi)$ in Eq. (3) the desired beam pattern is obtained. Taking the pattern synthesis step into consideration, we can express the beamformer filter weights $\mathbf{w}(\varphi)$ for the 3×3 2D-AVS URA in matrix form as

$$\mathbf{w}^H(\varphi) = \bar{\mathbf{b}}^T(\varphi)\mathbf{D}\mathbf{K}^{-1}\mathbf{G}. \tag{19}$$

III. PERFORMANCE

A. Directivity

The 2D directivity index (DI) of this beamformer is given in decibels by[27]

$$\mathrm{DI} = 10\log_{10} 2\pi \left[\int_0^{2\pi} |\mathcal{B}(\phi)|^2 \, d\phi \right]^{-1}. \tag{20}$$

Substituting Eq. (4) in Eq. (20), we obtain

$$\mathrm{DI} \approx 10\log_{10}(2N+1) \tag{21}$$

by analogy with the conventional ULA of $2N+1$ elements. For $N=5$, the value of DI is $\sim$10.4 dB. It is immediate from Eq. (4) that the 3 dB beamwitdth of the beamformer is $\sim 29.09^\circ$ and the first sidelobe, which occurs at $\phi = \varphi \pm 46.94^\circ$, is -13.02 dB relative to the main lobe.

Figure 3 shows the beam pattern obtained by using the proposed method. The main lobe is steered at 60°. It is worth noting that the beam pattern available in practice

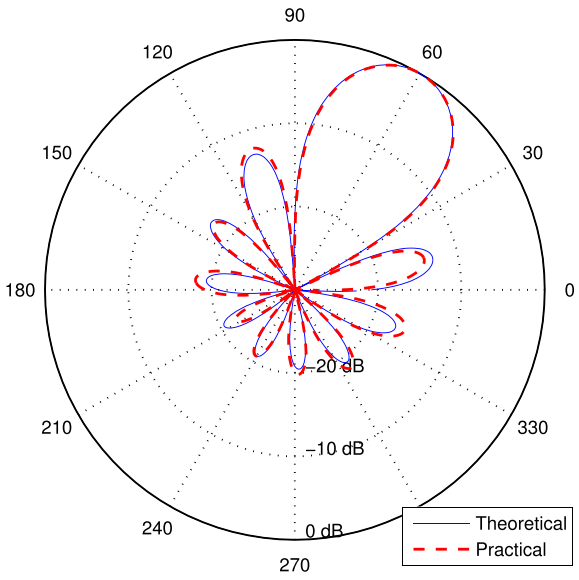

FIG. 3. (Color online) A comparison of the practical beam pattern with the theoretical beam pattern. The steering angle is 60°. The practical beam pattern is given by the thick dashed curve and the theoretical beam pattern by the thin solid curve.

$\mathcal{B}(\phi) = \mathbf{w}(\varphi)^H \mathbf{v}(\phi)$ is not equal to the theoretical beam pattern given by Eq. (4). Therefore, in this paper, $\mathcal{B}(\phi) = \mathbf{w}(\varphi)^H \mathbf{v}(\phi)$ is referred to as the "practical" beam pattern to distinguish it from the theoretical one. The theoretical beam pattern is also provided in Fig. 3 for comparison purposes. A small divergence of the side lobes of the practical beam pattern from the theoretical one can be observed in this case. The reason for this small difference is that the practically obtained acoustic modes are only approximations of the theoretical modes. Hence, the synthesized beam pattern presents errors. These errors are small, but they appear more significant compared to the side lobe magnitudes than to the magnitude of the main lobe.

The DI is also computed in Fig. 4. It can be noticed that the DI is almost frequency independent at low frequencies, i.e., for $a/\lambda < 1/2\pi$. Hence, in this paper, the required condition $a/\lambda \ll 1$ can be understood as $a/\lambda < 1/2\pi$.

B. WNG

Superdirective arrays are known to be sensitive to the spatially uncorrelated noise. In contrast to the ambient noise, this kind of noise is mainly due to nonacoustic causes, e.g., the self-noise of the sensor. The WNG is a widely used measure of robustness of a beamformer against the spatially uncorrelated noise given by[27]

$$\mathrm{WNG} = 1/\|\mathbf{w}(\varphi)\|^2, \tag{22}$$

where $\|\cdot\|$ denotes the Euclidean norm of a vector. Figure 5 plots the WNG of the proposed beamformer for different orders N. The WNG is evaluated numerically versus a/λ. The maximum response axis is steered at 60°. It is clearly shown that the WNG is dependent both on the frequency and the order N. One can observe that, especially at low-frequencies, reducing N by 1 improves radically the WNG. This is due to the fact that the subtractions of the observations across the sensors intrinsically decrease the power of the desired signal, whereas the power of the spatially uncorrelated noise adds up. The higher order mode components of the incident wave are much weaker than those of lower orders, which decrease with the order of the mode n by a factor $(2\pi a/\lambda)^{n-1}$ (see, e.g., Ref. 29). The mode amplification step handles the imbalanced amplitudes of the mode components, at the cost of a sharp increase in the uncorrelated noise power.

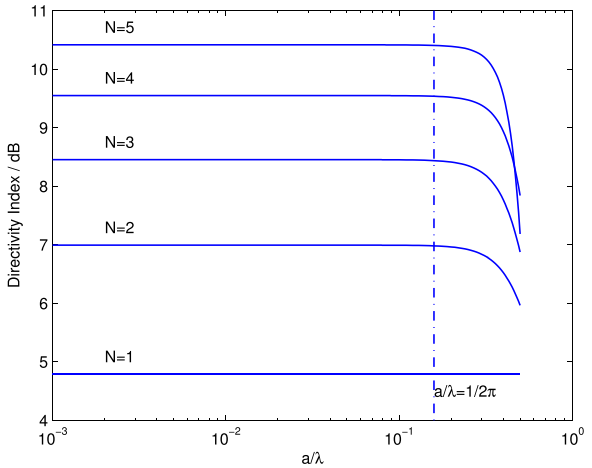

FIG. 4. (Color online) The directivity index versus the inter-sensor spacing in wavelengths. The beam is steered at 60° and the highest order of the modes is $N = 5$.

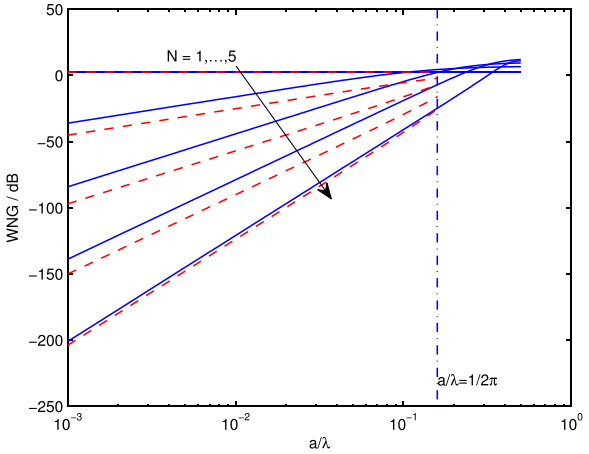

FIG. 5. (Color online) The WNG versus the inter-sensor spacing in wavelengths. The beam is steered at 60° and the highest order of the modes is $N = 5$. The solid line denotes the WNG of the proposed method applied to the 3×3 URA, whereas the dashed line denotes the results of Gur's method applied to a five-element ULA.

For comparison purposes, the WNG of Gur's subtractive beamformer for the ULA of 2D AVS[25] is also illustrated in Fig. 5. Let us take a closer look at the case $a/\lambda = 0.016$, for example. The values of the WNG for the two methods are tabulated in Table I. In the case of $N = 1$, both methods use only one AVS and, therefore, their WNGs is exactly the same. For $N = 2$ and $N = 3$, the proposed method yields a higher WNG because we choose the sensors with the largest possible spacing to extract the acoustic modes of order 2 and 3. When $N = 4$, this spacing advantage no longer holds. However, as more sensors are used, we still get a higher WNG. This advantage becomes even less significant for the case of $N = 5$.

It should be pointed out that all these comparisons are performed under the condition that the same DI is achieved for both URA and ULA. We observed that in some cases the higher WNG of the URA benefits from its larger inter-sensor spacing compared to the ULA. Although a larger inter-sensor spacing results in lower spatial correlation of the ambient noise measured across the sensors, it does not necessarily reduce the ambient noise rejection ability of the array. The reason is that the correlation of the desired signals between any two sensors is also reduced. As a matter of fact, the DI, which is an index that measures the ambient noise rejection ability of an array, is broadband constant as long as

TABLE I. The comparison of the two methods in terms of the WNG (dB) for $a/\lambda = 0.016$.

N	1	2	3	4	5
Proposed	2.5527	−12.0497	−36.0252	−66.6228	−104.6546
Gur	2.5527	−21.0371	−48.8274	−77.8534	−107.5202

$a/\lambda < 1/2\pi$, as it can be seen in Fig. 4. Hence, at low frequencies, increasing the inter-sensor spacing to obtain a higher WNG is always preferred until the array aperture reaches its limit.

Next, we examine analytically the influence of the WNG on the array gain (AG). Consider the simple case in which the ambient noise is isotropic. We denote the power of the correlated ambient noise by ε^2. Moreover, suppose that all the 2D AVSs are identical. Denote by σ^2 the power of the spatially uncorrelated noise and by μ the sensitivity of the AVS. Since $\varepsilon \gg \sigma$ and the self-noise of the pressure sensor is even smaller than the self-noise of the AVS in the underwater environment, the input signal-to-noise ratio (SNR) at each 2D AVS is given by

$$\mathrm{SNR}_i = \frac{\mu^2}{\mu^2\varepsilon^2 + \sigma^2} \approx \frac{1}{\varepsilon^2}.$$

The beamformer reduces the power of the ambient noise to $(\mu\varepsilon)^2/\mathrm{DI}$, but it also increases the self-noise to $\|\mathbf{w}(\varphi)\|^2\sigma^2$. Consequently, the SNR at the output end of the beamformer can be formulated by

$$\mathrm{SNR}_o = \frac{\mu^2}{\frac{(\mu\varepsilon)^2}{\mathrm{DI}} + \|\mathbf{w}(\varphi)\|^2\sigma^2}.$$

Then the AG can be expressed as

$$\mathrm{AG} = \frac{\mathrm{SNR}_o}{\mathrm{SNR}_i} \approx \frac{(\mu\varepsilon)^2}{\frac{(\mu\varepsilon)^2}{\mathrm{DI}} + \frac{\sigma^2}{\mathrm{WNG}}},$$

where we have used Eq. (22). This equation can be further reformulated as

$$\frac{1}{\mathrm{AG}} = \frac{1}{\mathrm{DI}} + \left(\frac{\sigma}{\mu\varepsilon}\right)^2 \frac{1}{\mathrm{WNG}}. \tag{23}$$

It is obvious that $\mathrm{WNG} < \mathrm{AG} < \min[\mathrm{DI}, (\mu\varepsilon/\sigma)^2\mathrm{WNG}]$.

As it can be seen in Eq. (23), the AG is dependent on the power ratio of the ambient noise and the spatially uncorrelated noise, ε^2/σ^2. Even though the power of the spatially uncorrelated noise σ^2 is often negligible compared with the ambient noise ε^2, the AG is low because the WNG of a superdirective array can be also very small, as shown in Fig. 5. Hence, the AVS of high quality, meaning small self-noise variance σ^2 and high sensitivity, is much preferred in the superdirective array design. If the quality of the AVS is not high enough such that $\mathrm{DI} \gg (\mu\varepsilon/\sigma)^2\mathrm{WNG}$, the AG becomes close to $(\mu\varepsilon/\sigma)^2\mathrm{WNG}$. In this case, as illustrated by Fig. 5, slightly reducing N can significantly increase the WNG. Thus, higher AG can be achieved at the cost of a mild decrease in the DI.

IV. EXPERIMENTS

A prototype of the 3×3 URA of 2D AVS has been developed at Harbin Engineering University, which allows us to test the proposed beamforming method in real-world experiments. The inter-sensor spacing a of this prototype is fixed to 0.12 m, such that the array aperture is constrained to <0.5 m.

The proposed method is tested first in an anechoic water tank. A sound source is fixed in the far field of the array, transmitting rectangular continuous wave pulses. The pulses are repeated every second and each pulse lasts 20 cycles in terms of the carrier frequency. At the receiver, the AVS array is rotated in the horizontal plane, which is equivalent to moving the source through all the possible azimuthal angles. The rotation stops every 5°. For each angle, we wait a little while before starting the measurements again in order to let the array return to the state of rest. Once the measurement starts, it takes 30 s before we rotate the array again with another 5°. Thus, 30 pulses are recorded for each incident angle.

Moreover, the rectangular pulses inevitably undergo some distortions due to the transmitting transducer and the receiving sensor. The distorted rising edge of the pulse may take several cycles before the pulse reaches the stable status. The falling edge of the pulse is mixed with some interference caused by the reverberant acoustic field. Therefore, a time window is used to truncate the received signals, conserving only the steady parts of the received pulses. For each incident angle, the magnitudes of the pulses at the beamformer output are averaged over 15 pulses (out of the 30 pulses) and squared; the result is taken as the power of the received pulse. The power of these pulses is further normalized by that of the pulse obtained from the main response axis. The power of the pulses is plotted versus the incident angles to generate the measured beam pattern. For example, the results for the frequency bin of 170 Hz are shown in Fig. 6; the main response axis is steered at direction 0°. It can be observed that the measured beam patterns, denoted by the discrete squares, are in good agreement with the theoretical beam patterns for $N=2$ and $N=3$. When the 4th order modes are used to synthesize the beam pattern, the measured side lobes start to diverge slightly from the theoretical side lobes. This phenomenon is even more obvious when N is increased to 5. This is mainly due to the fact that the WNG decreases drastically while N goes up, as shown in Fig. 5. In other words, this 5th order array is too sensitive for frequencies below 170 Hz. In this case, better results could be obtained by reducing N.

Figure 7 shows the beam patterns measured at 200 Hz. The results are similar to those obtained at 170 Hz. A close comparison of the beam patterns obtained at 170 Hz and at 200 Hz for $N=4$ and $N=5$ shows that the beam patterns obtained at 200 Hz are even less accurate than the ones obtained at 170 Hz. This is somewhat misleading as the WNG at 200 Hz should be higher. A possible explanation is that the sensitivity of the AVS that we used is not completely constant over the low frequencies. It is lower at 200 Hz than at 170 Hz. According to Eq. (23), the AG also decreases with the sensitivity of the AVS. Hence, a performance loss at 200 Hz is observed.

In mid-November 2013, we have carried out several experiments in Qiandao Lake in southern China. The water

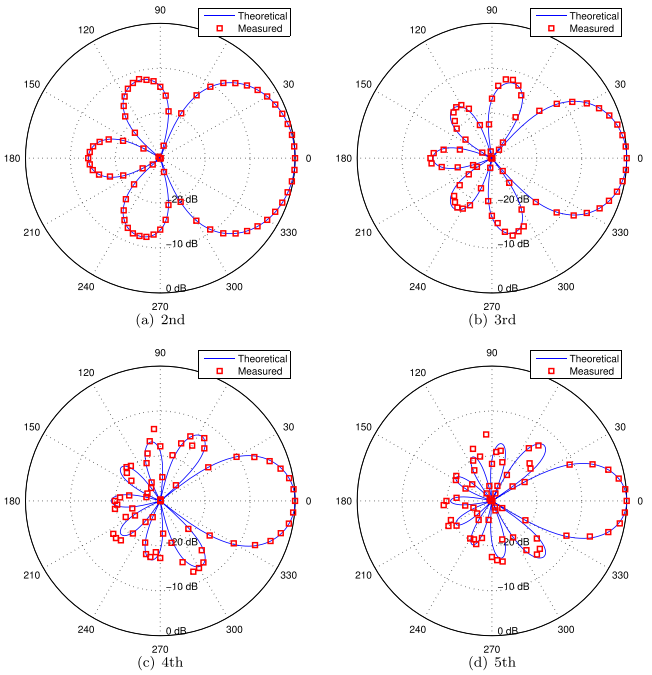

FIG. 6. (Color online) The beam patterns measured (the red squared markers) in the water tank at 170 Hz for $2 \leq N \leq 5$. The theoretical beam patterns (the thin blue curves) are also illustrated for comparison purposes.

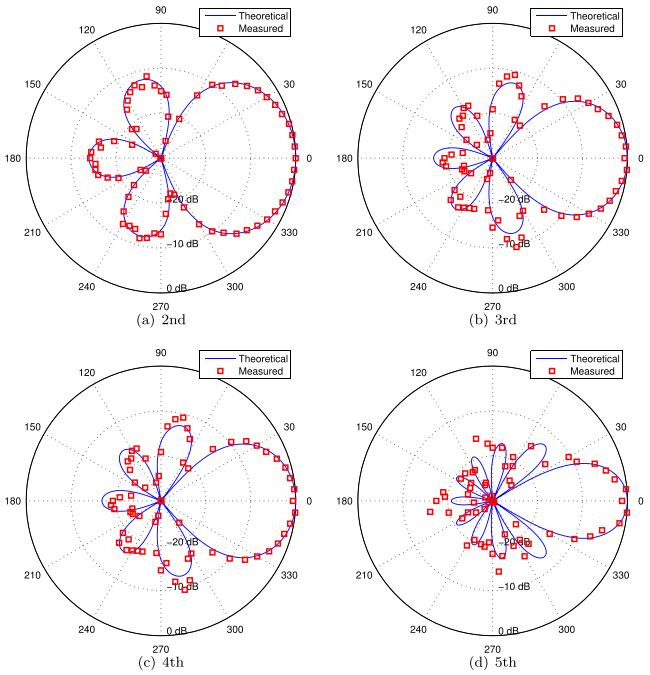

FIG. 8. (Color online) The beam patterns measured in the lake at 200 Hz for $2 \leq N \leq 5$; the other settings are similar to Fig. 6.

tank experiment setup is largely reproduced in the lake except that, to save time, during some of these experiments, the array was not necessarily rotated with a 5° angular step. For example, Figs. 8 and 9 show some of the beamforming results obtained at 200 and 300 Hz, respectively. The theoretical beam patterns are also illustrated for comparison purposes. It is clearly shown that, by using the proposed superdirective beamformer, directional responses can be obtained in practice with this miniaturized 3×3 URA of 2D AVS. Comparing these results to those obtained in the anechoic water tank, we can see that the measured beam patterns from the lake diverge more from the theoretical beam patterns. The main reason for this is that the acoustic environment in the lake is much more complex than in the water tank. The assumption of isotropy of the ambient noise is probably violated.

We arrive at the conclusion that for low frequencies, and given the type of 2D AVS that we used, the maximum

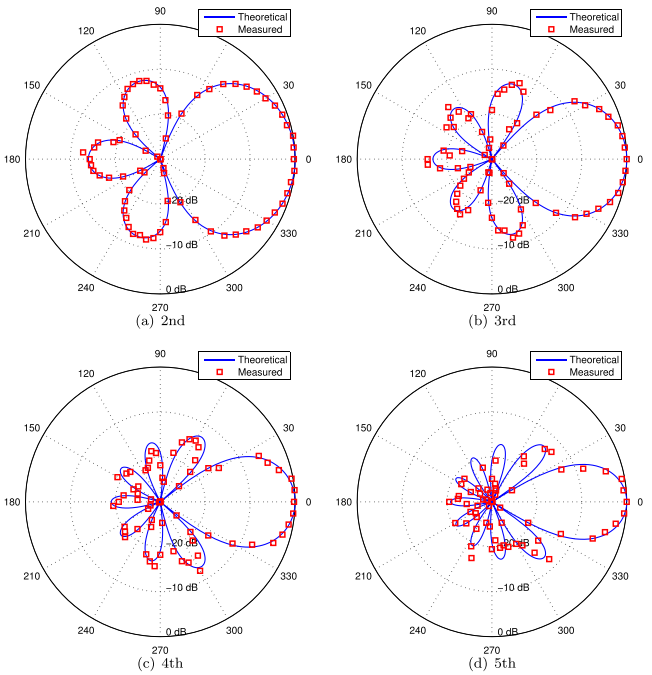

FIG. 7. (Color online) The beam patterns measured in the water tank at 200 Hz for $2 \leq N \leq 5$; the other settings are similar to Fig. 6.

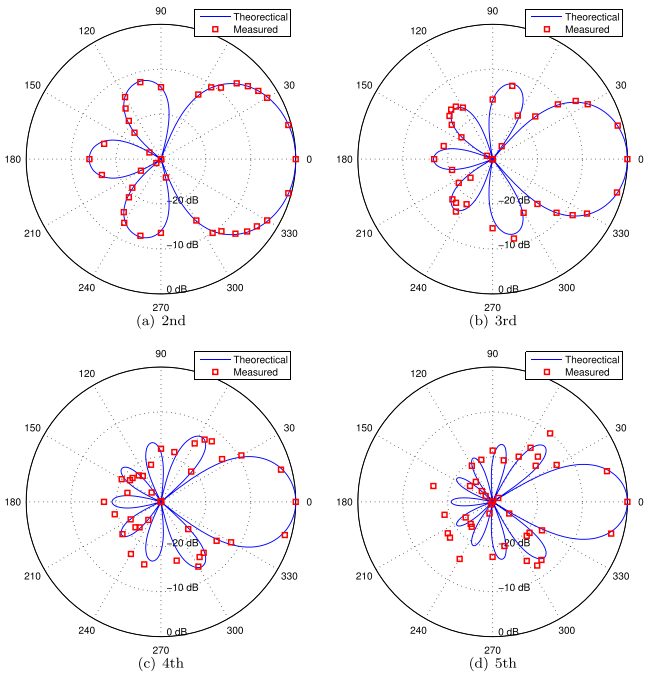

FIG. 9. (Color online) The beam patterns measured in the lake at 300 Hz for $2 \leq N \leq 5$; the other settings are similar to Fig. 6.

order of the modes for pattern synthesis should be constrained to $N \leq 4$, to ensure robustness of the superdirective 3×3 URA of 2D AVS.

V. CONCLUDING REMARKS

In this paper, a mode domain beamformer design is proposed for a miniaturized 3×3 URA of 2D AVS. This method uses the finite differences of the particle velocity observations to extract the directional acoustic modes, which are then synthesized in order to obtain the desired beam pattern. To validate this method, both laboratory and lake experiments have been carried out. It is shown that our approach readily provides a practical solution to low-frequency beamforming with a directivity index around 10.4 dB. The proposed method is limited to the use of the 3×3 URA of 2D AVS and the maximum order of the modes for pattern synthesis seems to be five. The analytical analysis and the experimental results indicate that an extension of the proposed approach to a 4×4 or larger scale array for higher order mode beamforming is less interesting. Moreover, when the quality of the 2D AVS is poor, higher AG can be achieved by reducing the maximum order of the modes.

ACKNOWLEDGMENTS

The authors acknowledge the support of the National Natural Science Foundation of China under Grant No. 11304251, the Specialized Research Fund for the Doctoral Program of Higher Education of China under Grant No. 20136102120014, and the Northwestern Polytechnical University Foundation for Fundamental Research under Grant No. JCY20130106 for funding this research. The authors also wish to thank Professor Hongjuan Chen, Professor Shengchun Piao, and their group members of Harbin Engineering University, who developed the prototype and successfully carried out the reported experiments, and the anonymous reviewers for their constructive comments and useful suggestions.

APPENDIX A: RELATION BETWEEN THE FINITE DIFFERENCES OF THE PARTICLE VELOCITIES AND THE TAYLOR'S SERIES MULTIPOLES

It can be seen from Eq. (1) that the 1st order mode components $\cos\phi$ and $\sin\phi$ can be obtained directly from the particle velocity at the origin. Thus, we only need to use the 2D AVS at the center of the array alone to extract the 1st order mode components; the chosen AVS is highlighted in Fig. 2(a). Readers are referred to Ref. 26 for the analogy between Fig. 2(a) and the source-sink picture of the monopole. In accordance, the coefficients are given by

$$g_{\ell,1}^{(1)} = \begin{cases} 1, & \ell = 5; \\ 0, & \text{otherwise} \end{cases}$$

for $\forall \ell \in \mathcal{L}$. These coefficients form the set $\mathcal{S}_1^{(1)}$. The elements of the other set $\mathcal{S}_2^{(1)}$ are simply given by $g_{\ell,2}^{(n)} = 0$ for $\forall \ell \in \mathcal{L}$. In this case, we obtain

$$\mathbf{M}^{(1)} = \begin{bmatrix} 1 & 0 \\ 0 & 1 \end{bmatrix}.$$

It follows from Eq. (6) that $u_1^{(1)} = \cos\phi$ and $u_2^{(1)} = \sin\phi$, which *are* the desired 1st order mode components.

By analogy with the source-sink picture of a dipole,[26] we derive the estimates of the cosine and the sine components of the 2nd order mode. In the 2D setup, there are only two forms of dipoles. Correspondingly, two sets of coefficients, $\mathcal{S}_1^{(2)}$ and $\mathcal{S}_2^{(2)}$, are obtained for the 2D-AVS array. Figures 2(b) and 2(f) illustrate the 2D AVS with their respective coefficients under the two cases. Figure 2(b) corresponds to the first case where the coefficients are given by the set $\mathcal{S}_1^{(2)}$. The 2D AVS associated with the two nonzero coefficients forms a subarray along the x axis and the particle velocity measurements made at the two positions are subtracted. The array factor of this subarray (i.e., the array response obtained as if the responses of all the array elements is omnidirectional[27]) is exactly the (1,1) element of the matrix $\mathbf{M}^{(2)}$, given by

$$m_{11}^{(2)} = j\sin(ka\cos\phi) \approx \kappa\cos\phi,$$

where $\kappa = jka$ and we have used $\sin x \approx x$ for small x to obtain the above approximation. This is justified because, herein, ka is very small. Analogously, in the case of $\mathcal{S}_2^{(2)}$, we obtain

$$m_{12}^{(2)} = -j\sin(ka\sin\phi) \approx -\kappa\sin\phi.$$

which is the array factor of the 2D-AVS subarray corresponding to the coefficient set $\mathcal{S}_2^{(2)}$. It is immediate from Eq. (7) that

$$\mathbf{M}^{(2)} \approx \begin{bmatrix} \kappa\cos\phi & -\kappa\sin\phi \\ \kappa\sin\phi & \kappa\cos\phi \end{bmatrix}.$$

Substituting it into Eq. (6), we obtain $u_1^{(2)} \approx \kappa\cos 2\phi$ and $u_2^{(2)} \approx \kappa\sin 2\phi$.

To obtain the 3rd order mode components $\cos 3\phi$ and $\sin 3\phi$, we use the quadrupole. The Taylor's series quadrupoles include two forms of axial quadrupoles along the two orthogonal axes and a lateral quadrupole in the 2D case.[26] The two Taylor's series axial quadrupoles can be merged to form another form of quadrupole (see Ref. 26 for the details). We base the choice of the coefficient set $\mathcal{S}_1^{(3)}$ on this quadrupole. Figure 2(c) shows the 2D AVS array in this case. The 2D AVS with nonzero coefficients form a lager subarray than in the 2nd order mode case. The array factor now is given by

$$\begin{aligned} m_{11}^{(3)} &= 4\cos(ka\cos\phi) - 4\cos(ka\sin\phi) \\ &\approx -2(ka)^2(\cos^2\phi - \sin^2\phi) = 2\kappa^2\cos 2\phi, \end{aligned}$$

where we have used the approximation

$$\cos x \approx 1 - \frac{x^2}{2}$$

for small values of x. The other set of coefficients $\mathcal{S}_2^{(3)}$ are determined in light of the source-sink picture of the Taylor series lateral quadrupole.[26] The coefficient set $\mathcal{S}_2^{(3)}$ is illustrated with the 2D-AVS URA in Fig. 2(g). Thus, another subarray is obtained with the array factor

$$\begin{aligned} m_{12}^{(3)} &= -(2j)^2 \sin(ka\sin\phi)\sin(ka\cos\phi) \\ &\approx -2\kappa^2 \sin 2\phi, \end{aligned}$$

leading to

$$\mathbf{M}^{(3)} \approx \begin{bmatrix} 2\kappa^2\cos 2\phi & -2\kappa^2\sin 2\phi \\ 2\kappa^2\sin 2\phi & 2\kappa^2\cos 2\phi \end{bmatrix}.$$

Using Eq. (6), we obtain that $u_1^{(3)} \approx 2\kappa^2\cos 3\phi$ and $u_2^{(3)} \approx 2\kappa^2\sin 3\phi$.

In a similar way we can obtain the 4th and the 5th order mode components. For the 4th order modes, we use the Taylor's series octapoles[26] to determine the coefficients. There are two forms of octapoles in the 2D case. The corresponding coefficient sets are illustrated by Figs. 2(d) and 2(h). By similar arguments, we obtain

$$\begin{aligned} m_{11}^{(4)} &= 4j\sin(ka\cos\phi)(1-\cos(ka\sin\phi)) \\ &\approx -2\kappa^3\cos\phi\sin^2\phi, \\ m_{12}^{(4)} &= 4j\sin(ka\sin\phi)(1-\cos(ka\cos\phi)) \\ &\approx -2\kappa^3\sin\phi\cos^2\phi, \end{aligned}$$

which yield

$$\mathbf{M}^{(4)} \approx \begin{bmatrix} -2\kappa^3\cos\phi\sin^2\phi & -2\kappa^3\sin\phi\cos^2\phi \\ 2\kappa^3\sin\phi\cos^2\phi & -2\kappa^3\cos\phi\sin^2\phi \end{bmatrix}.$$

It follows that $u_1^{(4)} \approx (1/2)\kappa^3(-1+\cos 4\phi)$ and $u_2^{(4)} \approx (1/2)\kappa^3\sin 4\phi$.

The differential of the Talyor's series octapole with respect to either axis produces the 4th order multipole. The coefficient set $\mathcal{S}_1^{(5)}$ can be obtained in light of such a 4th order multipole. Figure 2(e) shows the 2D AVS associated with the coefficients of $\mathcal{S}_1^{(5)}$. In this case, all 2D AVS are associated with nonzero coefficients. That is, all of them are used to estimate the 5th order mode components. The array factor is given by

$$\begin{aligned} m_{11}^{(5)} &= -4(1-\cos(ka\cos\phi))(1-\cos(ka\sin\phi)) \\ &\approx -\kappa^4\cos^2\phi\sin^2\phi. \end{aligned}$$

It is not clear whether there also exists another form of 4th order multipole that can be described by nine point sources and sinks on the 3×3 grid. In other words, we have no clue how to obtain the second nontrivial coefficient set $\mathcal{S}_2^{(5)}$ for this 3×3 2D-AVS URA yet. Hence, we simply set the differential coefficients $g_{\ell,2}^{(5)} = 0$ for all $\ell \in \mathcal{L}$. Then, we obtain

$$m_{12}^{(5)} = 0$$

and, as a consequence, the matrix

$$\mathbf{M}^{(5)} \approx \begin{bmatrix} -\kappa^4\cos^2\phi\sin^2\phi & 0 \\ 0 & -\kappa^4\cos^2\phi\sin^2\phi \end{bmatrix}.$$

Once again, using Eq. (6) we get $u_1^{(5)} \approx (1/16)\kappa^4(-2\cos\phi + \cos 3\phi + \cos 5\phi)$ and $u_2^{(5)} \approx (1/16)\kappa^4(-2\sin\phi - \sin 3\phi + \sin 5\phi)$.

This approach ends with $N=5$ and whether it can be extended for the higher order modes remains unclear at the current stage. In practice, it is not so interesting to extract the higher order modes because the method becomes too sensitive if $N\geq 5$. This has been demonstrated in Sec. III.

It should be noted that for $1\leq n\leq 5$, the estimates $u_1^{(n)}$ and $u_2^{(n)}$ consist only of the cosine or the sine mode components, respectively. In addition, for the 4th and the 5th order modes, the estimates also have undesired lower order mode components. In other words, other than the nth order mode components, the estimate $u_q^{(n)}$ also contains the undesired $(n-2\ell)$th order mode components for $1\leq\ell\leq\lfloor n/2\rfloor$, where $\lfloor\cdot\rfloor$ denotes the integer part of a number. This phenomenon can be seen as "coupling" between the modes due to the finite difference errors. For instance, $u_1^{(5)}$ is such a mixture. We can further deduce that the estimate $u_q^{(n)}$ contains the 0th order mode *only if* n is even and $q=1$, e.g., $u_1^{(4)}$.

APPENDIX B: PROOF OF THE SECOND PROPERTY OF THE DECOUPLING MATRIX

We base the proof of the second property on the following lemma.

Lemma: If a lower triangular matrix $\mathbf{R}$ has the property that its (ℓ,k) elements are nonzero only if $\ell-k$ is even, its inverse $\mathbf{D}=\mathbf{R}^{-1}$ has the same property.

Proof: It is clear that the (ℓ,k) elements of $\mathbf{R}$ are zeros if $\ell-k$ is odd. The lemma is proved if we can show that for any ℓ,k satisfying $\ell>k$ and $\ell-k$ is odd, the (ℓ,k) element of $\mathbf{D}$, denoted by $d_{\ell,k}$, is also zero. It is known that[30]

$$d_{\ell,k} = \frac{(-1)^{\ell+k} r_{k,\ell}^m}{\det(\mathbf{R})}, \tag{B1}$$

where $\det(\mathbf{R})$ is the determinant of the matrix $\mathbf{R}$ and $r_{k,\ell}^m$ is the (k,ℓ) minor of $\mathbf{R}$, i.e., the determinant of the $(n-1)\times(n-1)$ matrix that results from deleting row k and column ℓ of $\mathbf{R}$. We denote this $(n-1)\times(n-1)$ matrix by $\mathbf{R}_{k,\ell}$, which is also a lower triangular matrix. Hence, the determinant of the lower triangular matrix $\mathbf{R}_{k,\ell}$, i.e., the minor $r_{\ell,k}^m$, equals the product of the diagonal elements of the matrix $\mathbf{R}_{k,\ell}$.[30] It is obvious that the (k,k) element of $\mathbf{R}_{k,\ell}$ is $r_{k+1,k}$, which is a zero. Moreover, all the next $\ell-k-1$ diagonal elements of $\mathbf{R}_{k,\ell}$, which are denoted by $r_{k+2,k+1},\ldots,r_{\ell,\ell-1}$, are also equal to zero. Therefore, the minor $r_{\ell,k}^m = 0$. Substituting it into Eq. (B1), we obtain $d_{\ell,k}=0$. The proof is complete.

It is immediate from this lemma that the second property holds true.

[1]J. Meyer and G. Elko, "A highly scalable spherical microphone array based on an orthonormal decomposition of the soundfield," in *Proc. IEEE ICASSP*, Orlando, FL (May 2002), Vol. 2, pp. 1781–1784.
[2]B. Rafaely, "Anaysis and design of spherical microphone arrays," IEEE Trans. Speech Audio Process. **13**(1), 135–143 (2005).
[3]Z. Li and R. Duraiswami, "Flexible and optimal design of spherical microphone arrays for beamforming," IEEE Trans. Audio, Speech, Language Process. **15**(2) 702–714 (2007).
[4]H. Sun, S. Yan, and U. P. Svensson, "Robust minimum sidelobe beamforming for spherical microphone arrays," IEEE Trans. Audio, Speech, Language Process. **19**(4), 1045–1051 (2011).
[5]S. Yan, H. Sun, U. P. Svensson, X. Ma, and J. M. Hovem, "Optimal modal beamforming for spherical microphone arrays," IEEE Trans. Audio, Speech, Language Process. **19**(2), 361–371 (2011).
[6]H. Teutsch and W. Kellermann, "Acoustic source detection and localization based on wavefield decomposition using circular microphone arrays," J. Acoust. Soc. Am. **120**(5), 2724–2736 (2006).
[7]A. M. Torres, M. Cobos, B. Pueo, and J. J. Lopez, "Robust acoustic source localization based on modal beamforming and time-frequency processing using circular microphone arrays," J. Acoust. Soc. Am. **132**(3), 1511–1520 (2012).
[8]T. D. Abhayapala and A. Gupta, "Higher order differential-integral microphone arrays," J. Acoust. Soc. Am. **127**(5), EL227–EL233 (2010).
[9]S. Doclo and M. Moonen, "Superdirective beamforming robust against microphone mismatch," IEEE Trans. Audio, Speech, Language Process. **15**(2), 617–631 (2007).
[10]E. De Sena, H. Hacihabiboglu, and Z. Cvetkovic, "On the design and implementation of higher order differential microphones," IEEE Trans. Audio, Speech, Language Process. **20**(1), 162–174 (2012).
[11]J. Chen, J. Benesty, and C. Pan, "On the design and implementation of linear differential microphone arrays," J. Acoust. Soc. Am. **136**(6), 3097–3113 (2014).
[12]Y. Yang, C. Sun, and C. Wan, "Theoretical and experimental studies on broadband constant beamwidth beamforming for circular arrays," in *Proc. OCEANS*, San Diego, CA (Sept. 2003), Vol. 3, pp. 1647–1653.
[13]Y. Ma, Y. Yang, Z. He, K. Yang, C. Sun, and Y. Wang, "Theoretical and practical solutions for high-order superdirectivity of circular sensor arrays," IEEE Trans. Ind. Electron. **60**(1), 203–209 (2013).
[14]Y. Wang, Y. Yang, Y. Ma, and Z. He, "Robust high-order superdirectivity of circular sensor arrays," J. Acoust. Soc. Am. **136**(4), 1712–1724 (2014).
[15]A. Trucco, F. Traverso, and M. Crocco, "Broadband performance of superdirective delay-and-sum beamformers steered to end-fire," J. Acoust. Soc. Am. **135**(6), EL331–EL337 (2014).
[16]B. A. Cray, V. M. Evora, and A. H. Nuttall, "Highly directional acoustic receivers," J. Acoust. Soc. Am. **113**(3), 1526–1532 (2003).
[17]D. J. Schmidlin, "Directionality of generalized acoustic sensors of arbitrary order," J. Acoust. Soc. Am. **121**(6), 3569–3578 (2007).
[18]J. A. McConnell, S. C. Jensen, and J. P. Rudzinsky, "Forming first- and second-order cardioids with multimode hydrophones," in *Proc. OCEANS*, Boston, MA (Sept. 2006).
[19]J. C. Nickles, G. Edmonds, R. Harriss, F. Fisher, W. S. Hodgkiss, J. Giles, and G. D'Spain, "A vertical array of directional acoustic sensors," in *Proc. OCEANS*, Newport, RI (Oct. 1992), Vol. 1, pp. 340–345.
[20]J. C. Shipps and B. M. Abraham, "The use of vector sensors for underwater port and waterway security," in *Proc. Sensors Industry Conf.*, New Orleans, LA (Jan. 2004), pp. 41–44.
[21]M. T. Silvia and R. T. Richards, "A theoretical and experimental investigation of low-frequency acoustic vector sensors," in *Proc. OCEANS*, Biloxi, MS (Oct. 2002), Vol. 3, pp. 1886–1897.
[22]J. F. McEachern, J. A. McConnell, J. Jamieson, and D. Trivett, "ARAP—Deep ocean vector sensor research array," in *Proc. OCEANS*, Boston, MA (Sept. 2006).
[23]G. L. D'Spain, J. C. Luby, G. R. Wilson, and R. A. Gramann, "Vector sensors and vector sensor line arrays: Comments on optimal array gain and detection," J. Acoust. Soc. Am. **120**(1), 171–185 (2006).
[24]N. Zou and A. Nehorai, "Circular acoustic vector-sensor array for mode beamforming," IEEE Trans. Signal Process. **57**(8), 3041–3052 (2009).
[25]B. Gur, "Particle velocity gradient based acoustic mode beamforming for short linear vector sensor arrays," J. Acoust. Soc. Am. **135**(**6**), 3463–3473 (2014).
[26]J. P. Wikswo and K. R. Swinney, "A comparison of scalar multipole expansions," J. Appl. Phys. **56**(11), 3039–3049 (1984).
[27]H. L. Van Trees, *Optimum Array Processing: Part IV of Detection, Estimation, and Modulation Theory* (Wiley, New York, 2002), Chap. 4, pp. 231–331.
[28]J. A. Clark, "Modal beam processing of acoustic vector sensor data," U.S. patent 7,839,721 B1 (November 23, 2010).
[29]L. E. Kinsler, A. R. Frey, A. B. Coppens, and J. V. Sanders, *Fundamentals of Acoustics*, 4th ed. (Wiley, New York, 2000), Chap. 5, pp. 113–148.
[30]G. H. Golub and C. F. Van Loan, *Matrix Computations*, 3rd ed. (The Johns Hopkins University Press, Baltimore, MD, 1996), Chap. 3, pp. 87–132.